

# Constraining corotation from shocks in tightly-wound spiral galaxies

D. M. Gittins<sup>1\*</sup> and C. J. Clarke<sup>1†</sup>  
<sup>1</sup>*Institute of Astronomy, Madingley Road, Cambridge CB3 0HA*

7 July 2018

## ABSTRACT

We present a new method for estimating the corotation radius in tightly wound spiral galaxies, through analysis of the radial variation of the offset between arms traced by the potential (P-arms) and those traced by dust (D-arms). We have verified the predictions of semi-analytical theory through hydrodynamical simulations and have examined the uniqueness of the galactic parameters that can be deduced by this method. We find that if the range of angular offsets measured at different radii in a galaxy is greater than around  $\pi/4$ , it is possible to locate the radius of corotation to within  $\sim 25\%$ . We argue that the relative location of the P- and D-arms provides more robust constraints on the galactic parameters than can be inferred from regions of enhanced star formation (SF-arms), since interpretation of the latter involves uncertainties due to reddening and the assumed star formation law. We thus stress the importance of K-band studies of spiral galaxies.

**Key words:** hydrodynamics – methods: numerical – galaxies: ISM – galaxies: spiral – galaxies: structure

## 1 INTRODUCTION

Theories of the structure, origin, development and effects of spiral arms in galaxies have occupied researchers ever since such structure was discovered in 1845. Many galaxies are observed with tightly-wound, regular spiral arms covering a significant fraction of their disc. The commonest model of this phenomenon is based on the Lin-Shu hypothesis of spiral structure (Lin, Yuan & Shu 1969), which states that quasi-steady spiral patterns exist in the stellar disc, rotate at a pattern speed  $\Omega_P$ , and persist for many orbits. The orbits of the stars are organised into ‘kinematic density waves’, which increase the stellar density in a spiral pattern. The stars themselves drift through the pattern inside the corotation radius, as they orbit with an angular velocity  $\Omega > \Omega_P$ .

The spiral density wave picture is by no means the only theory of spiral structure, but provides a very successful description. The possible origins, driving mechanisms and long-term support of such density waves has been the subject of a great deal of literature, and this subject is beyond the scope of this paper; see reviews by Kaplan & Pikelner (1974) and Toomre (1977). It is generally accepted that spiral waves, if they do not naturally arise through instabilities, may be driven by nearby companions or central bars, and that under the right conditions they may persist for many

rotations, and it is from this starting point that we proceed in this paper.

Galaxies that are optically classified as spirals usually have a clear spiral structure with one dominating mode, and arms are usually logarithmic in shape (e.g. they have a constant pitch angle) (Kennicutt 1981; Kennicutt & Hodge 1982; García Gómez & Athanassoula 1993; Ma 2002). However, galaxies not classified as spirals are now known commonly to show spiral structure in their stellar discs. The old stellar population, which will trace the mass of the disc, can be observed in longer wavelengths such as the K or K’ bands. Schweizer (1976) found ‘broad spiral patterns’ in the discs of six spiral galaxies, concluding that smooth spiral structure exists in their mass distributions. Elmegreen & Elmegreen (1984) examined several galaxies of different types, suggesting a class of galaxy which has flocculent structure at blue wavelengths and a spiral structure in K. More recently, Block et al. (1994) showed that optical classification does not constrain the structure of stellar discs, finding smooth spiral structure in galactic discs independently of their optical structure. Many galaxies optically classified as flocculent, when observed in K’, show regular spiral structure (Thornley 1996; Grosbøl & Patsis 1998; Seigar et al. 2003). Most of these have a central bar, and some also have a neighbour (Seigar, Chorney & James 2003). The presence of regular spiral structure, but flocculent structure in bluer wavelengths, has also arisen in numerical simulations (Berman 2002). We make the distinction between three separate arm

\* Email: dgittins@ast.cam.ac.uk

† Email: cclarke@ast.cam.ac.uk

components: the peaks of the underlying stellar mass distribution, approximately tracing the perturbations in the gravitational Potential (the P-arms), the shock fronts of the gas, which will generally be observed from Dust (the D-arms), and the ridges of enhanced Star Formation (the SF-arms).

Many tightly-wound spiral galaxies are known. Assuming that the model of a rotating spiral potential is accurate, the parameters of that potential are fundamental to the galaxies themselves. An understanding of the structure of spiral arms is important in considering the processes affecting the ISM flowing through them. In this paper, we focus on the determination of the corotation radius.

We discuss the formation of single-shock flows in the gaseous disc, and show how the angular offset between these shocks (the D-arms) and the minima of the gravitational potential (the P-arms) could be used to constrain corotation. In section 2, we introduce the model spiral potential, to which the gas responds. Section 3 investigates the resulting gas flow using a well known semi-analytical approach, and compares the results to those obtained by numerical methods. In section 4, different components of spiral arms are discussed, and the offset function  $\Theta$  is introduced. Various ways to constrain corotation are summarised in section 5, and the use of the offset function to provide an additional constraint is explained. Finally, our findings are summarised in section 6.

## 2 MODEL SPIRAL POTENTIAL

The rigidly rotating potential of a spiral galaxy can be decomposed into a static, axisymmetric part and a spiral perturbation. We define the gravitational potential  $V$  (in galactocentric polar coordinates  $R, \theta$ ) as

$$V(R, \theta, t) = V_R(R) + V_S(R, \theta, t)$$

where  $V_R$  is the axisymmetric potential and  $V_S$  is the spiral perturbation.

The axisymmetric part represents the unperturbed velocity curve. In this paper, the following velocity curve is used:

$$v(R) = v_{\max} \sqrt{F_b \epsilon_b R \exp(-\epsilon_b R) + 1 - \exp(-\epsilon_d R)}$$

where  $v_{\max}$  is the limit of the circular velocity at large radius,  $\epsilon_d$  and  $\epsilon_b$  are the inverse disc and bulge scale lengths (respectively) and  $F_b$  is the bulge strength parameter (Contopoulos & Grosbøl 1986). The potential  $V_R$  that produces this velocity curve is

$$V_R(R) = v_{\max}^2 (\ln R + E_1(\epsilon_d R) - F_b e^{-\epsilon_b R})$$

where the exponential integral  $E_1$  is defined as

$$E_1(x) = \int_x^\infty \frac{e^{-u} du}{u}.$$

A spiral perturbation with one mode is given by the general form

$$V_S = A(R, t) \cos(\chi)$$

where the spiral phase  $\chi$  is defined as

$$\chi = \Phi(R) - m(\theta - \Omega_P t)$$

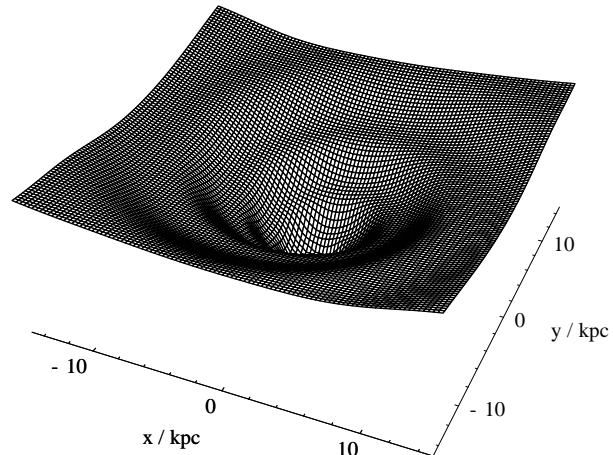


**Figure 1.** Potential surface with parameters  $F_b = 0$ ,  $\epsilon_d^{-1} = 1.5$  kpc,  $\epsilon_s^{-1} = 10$  kpc,  $\sin i = 0.2$ ,  $m = 2$  and  $F_0 = .6$  at  $R_0 = 8.5$  kpc. A very high value of  $F$  is chosen to produce a spiral perturbation visible on this figure.

and the pattern has  $m$  arms. The pattern rotates rigidly at angular velocity  $\Omega_P$ . The radial shape of the arms is set by the function  $\Phi(R)$ , and at constant radius, the potential is sinusoidal in  $\theta$  with period  $2\pi/m$ . The overall amplitude is set by  $A(R, t)$ . The equipotentials of each mode are spirals, which have an inclination  $i(R)$  to circles. Trailing logarithmic arms, with a constant inclination  $i$ , correspond the choice

$$\Phi(R) = -\frac{m}{\tan i} \ln(R)$$

It is convenient to define the perturbation strength  $F(R)$  as the ratio of the amplitude of the perturbation force to the axisymmetric force:

$$F = \frac{|\nabla V_S|_{\max}}{|\nabla V_R|} = \frac{mA}{v^2 \sin i}$$

where the circular velocity at radius  $R$  is  $v$ . The radial and time variation of the amplitude can be chosen arbitrarily. A suitable radial choice is to specify (Contopoulos & Grosbøl 1986)

$$A(R, t) = A_0 R \exp(-\epsilon_s R)$$

where  $\epsilon_s$  is the inverse spiral scale length, and the overall amplitude at any time is set by  $A_0$ . In this paper we are interested in steady solutions in which the potential has reached a stable state, so that  $A$  is independent of time.  $A_0$  can most conveniently be set by requiring that the maximum relative spiral strength takes a specified value  $F_0$  at some radius  $R_0$ .

An example potential surface, with an exaggerated spiral perturbation, is shown in figure 1.

## 3 RESPONSE OF GASEOUS DISC

A relatively small perturbation can have a significant effect on the flow of gas through it. Large deviations from the circular flow can lead to the formation of shocks. In this section we examine the formation of single-shock solutions

in the flow of isothermal gas through the spiral potential. Since the intent is to examine the large-scale behaviour, and ignore small-scale processes, approximations of initial uniformity and isothermality are appropriate. Here, the sound speed used is an ‘effective’ sound speed equal to the velocity dispersion of the ISM, a good approximation for the time and length scales involved (Cowie 1980).

### 3.1 Semi-analytical technique

In this paper we repeat the procedure used in Shu, Milione & Roberts (1973) for finding non-linear solutions (containing a shock) to the asymptotic equations of gas flow under a spiral perturbation. The derivation of the equations and descriptions of the procedure are given in Roberts (1969) and Shu et al. (1972) and are only briefly described here.

Solutions are expressed in ‘curvilinear’ coordinates  $(\eta, \xi)$  that vary perpendicularly to and parallel to the equipotentials, respectively (see figure 2). These are defined in a stationary frame of the spiral perturbation. They are defined by<sup>1</sup>

$$d\eta = -k dR + m d\theta$$

$$d\xi = -m \frac{dR}{R} - k R d\theta$$

where

$$k = \frac{\partial \Phi(R)}{\partial R} = \frac{-m}{R \tan i}$$

where the last result is for the case of logarithmic arms. A circle at constant  $R$  will therefore pass through  $m$  periods of  $\eta$ . Specifically we define

$$\eta = -\chi + \pi \quad (1)$$

so that  $\eta = 0$  always corresponds to the potential minimum. The passage from one arm to the next corresponds to a period of  $2\pi$  in  $\eta$ , regardless of the number of arms.

The velocity of the gas is written in components  $(u_\eta, u_\xi)$  in this coordinate system. These are then expressed as the sum of the ‘base’ flow  $(u_{\eta 0}, u_{\xi 0})$  (the equilibrium circular flow when the perturbation is not present, in the stationary frame of the perturbation) and a perturbed velocity  $(u_{\eta 1}, u_{\xi 1})$ . In the specific case of logarithmic arms the coordinates can be defined as follows:

$$\eta = \frac{m}{\tan i} \ln(\epsilon_s R) + m(\theta - \Omega_P t) + \pi$$

$$\xi = -m \ln(\epsilon_s R) + m \tan i (\theta - \Omega_P t).$$

The differential equations in  $u_\eta$  and  $u_\xi$ , and the technique for locating appropriate solutions, are given in appendix A. The boundary condition for any solution is that it be periodic in  $\eta$  with period  $2\pi$ . Solutions are found along streamlines under the approximation that they are at nearly constant radius, and the surface density  $\sigma$  is then found from the velocity. The solution at a given radius is controlled by seven parameters, under the approximation that they are constant along a streamline:

<sup>1</sup> These coordinates differ slightly to those in Shu et al. (1972) and Roberts (1969).

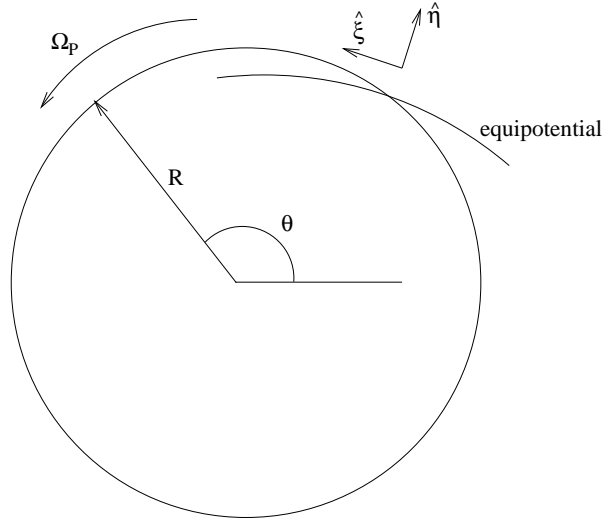


Figure 2. The coordinate system used in this paper.

- $m$  (the number of arms)
- $\Omega_P$  (the pattern speed of the arms)
- $i$  (the local pitch angle)
- $F$  (the local relative arm strength)
- $v$  (the unperturbed circular velocity)
- $\kappa$  (the local epicyclic frequency)
- $a$  (the effective sound speed of the gas)

Base-supersonic flow is defined as any flow with  $u_{\eta 0} > a$ , so that in the stationary frame of the arms, the unperturbed flow perpendicular to the equipotentials is supersonic. Similarly, base-subsonic flow has  $u_{\eta 0} < a$ . In general, if the flow in a galaxy is mostly base-supersonic, there will be a region (the base-subsonic region) in which it is not. This, of course, occurs either side of the corotation radius in a band where the relative velocity  $R(\Omega - \Omega_P)$  is sufficiently small. In this region, the response of the gas, and the asymptotic flow solutions, will be qualitatively different. The base-subsonic region is bounded by the radii satisfying  $R \sin i (\Omega - \Omega_P) = \pm a$ .

If for the whole solution  $u_\eta < a$  (entirely subsonic) or  $u_\eta > a$  (entirely supersonic), the solution will not contain a shock. This will occur under conditions where the sound speed  $a$  is very high or low, or the strength  $F$  of the perturbation is sufficiently small. In the limit of small  $F$ , the solutions reach the first-order response, which is sinusoidal in  $u$  and  $v$  (and hence  $\sigma$ ), such that  $u_\eta \propto -\cos \eta$  and  $u_\xi \propto \sin \eta$ . The maximum density (and minimum of  $u_\eta$ ) occur at the centre of the potential well, i.e. at  $\eta = 0$ .

If the strength  $F$  of the perturbation is gradually increased, starting from an entirely subsonic solution, then at some point the flow will be sufficiently perturbed that  $u_\eta$  will pass the sound speed  $a$ . Any solution must now contain a sonic point, at which the gas accelerates to supersonic velocities, and a shock. Such solutions are no longer symmetric. A consistent solution consists of a closed curve in the  $(u_\xi, u_\eta)$  plane containing a single isothermal shock, with a periodicity in  $\eta$  of  $2\pi$ . Such a solution only exists for certain choices of parameters.

Figure 3 shows an example velocity curve in  $(u_\xi, u_\eta)$  for a solution in a tightly wound spiral, and the corresponding density profile through the shock is shown in figure 4.

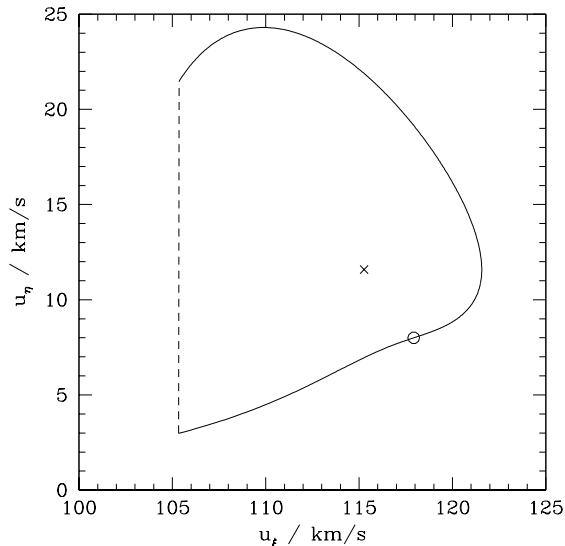


**Figure 3.** Velocity curve in  $(u_\xi, u_\eta)$  plane of the solution at  $R_0 = 8$  kpc and  $F = 0.05$ . The cross marks the unperturbed velocity. The sonic point is marked by a circle. The shock is represented by the dashed line.

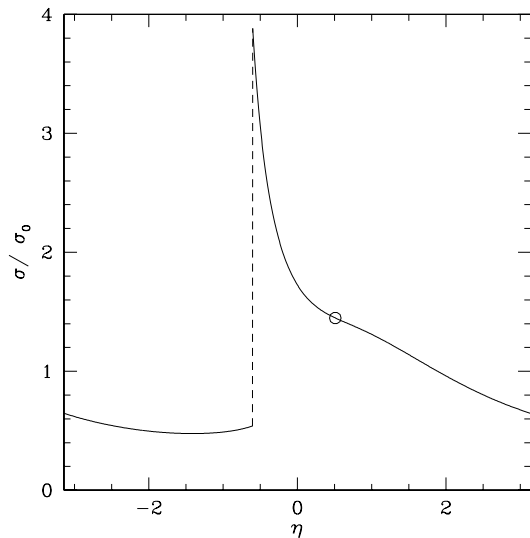


**Figure 4.** Surface density profile  $\sigma(\eta)$  corresponding to the solution shown in figure 3. The sonic point is marked by a circle.

### 3.1.1 Existence of a solution

It is not always possible to find solutions containing a shock for any choice of parameters. The equations are based on the approximation that the gravitational field is in the  $\eta$  direction (and hence that the shock is parallel to the equipotentials), which will hold for large  $|k|R$  or (equivalently)  $\sin i \ll 1$ , so that the spiral arms are tightly wound and  $\Phi(R)$  varies rapidly. In more open spirals the equations therefore break down. Also, the parameters are approximated as constant along a streamline, which will be a good approximation

**Table 1.** Parameter values of the standard model.

$F_b^{-1}$	0
$\epsilon_{d1}^{-1}$	1.5 kpc
$\epsilon_{s1}^{-1}$	10 kpc
$m$	2
$\sin i$	0.1
$\Omega_P$	$13 \text{ km s}^{-1} \text{ kpc}^{-1}$
$a$	$8 \text{ km s}^{-1}$
$F(R_0) \equiv F_0$	0.05
$v(R_0) \equiv v_0$	$220 \text{ km s}^{-1}$
$R_0$	8.5 kpc

only if  $F$  is not much larger than  $\sin i$ . In our experience, solutions are difficult or impossible to find for  $F \gtrsim 0.1$  and  $\sin i \gtrsim 0.2$  (with all other parameters as indicated in table 1).

Within parameters that satisfy these approximations, solutions still may not exist. In particular, solutions in the base-subsonic region are difficult to find, as discussed in appendix A. In many cases, although shock solutions can be found, no solution of the correct periodicity exists.

Many solutions show secondary peaks in the density. These occur especially near the ultraharmonic resonances, where higher harmonic terms in the solution become important. If a secondary peak crosses the sonic line, a second shock will occur. It will therefore become impossible to locate a single-shock solution, since a singularity will be present at the second sonic point. It is possible to extend the method described here to include a secondary shock (Shu et al. 1973), but this has not been attempted in this paper.

### 3.1.2 Results

A ‘standard model’ is defined, with parameter values as given in table 1. Density profiles for the standard model are shown in figure 5 for a range of radii. No profiles are shown for radii between 11 and 12.5 kpc, as no solutions exist. The figure shows the smooth transition toward the base-subsonic density profiles, in which the broad density peak at  $\eta = 0$  appears and the shock is small. This figure also indicates that the shock location moves to smaller values of  $\eta$  with increasing radius. At small radii, the shock occurs almost at the potential minimum, but as the radius increases and the shock becomes weaker, it moves upstream toward the potential maximum.

## 3.2 Numerical calculations

The response of an isothermal gas disc can be computed with numerical hydrodynamical codes. In this section, results obtained using two-dimensional Smoothed Particle Hydrodynamics (2D SPH) and a two-dimensional Piecewise Parabolic Method (PPM) code are compared with the results of the semi-analytical analysis. Numerical codes are not restricted by the approximations of the semi-analytical approach, nor to results containing a single shock, and should therefore be able to capture more detailed structure.

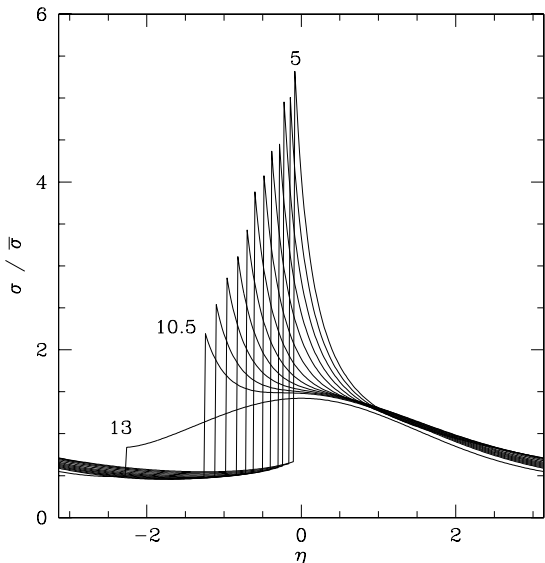


**Figure 5.** Density profiles  $\sigma(\eta)$  for the standard model, at radii from  $R = 5$  kpc to  $R = 10.5$  kpc (indicated) in steps of  $0.5$  kpc. The profile at  $R = 13$  kpc is also shown.

### 3.2.1 Two-dimensional Smoothed Particle Hydrodynamics

Calculations with 2D SPH showed a good general agreement to the results of the semi-analytical analysis, but did not resolve the sharp shocks accurately. A tendency for the SPH particles to ‘clump’ together unphysically was overcome by using a triquintic spline smoothing kernel, but this results in decreased spatial resolution (see Gittins 2003, for details). This problem may be alleviated by adjusting the time dependence of the smoothing lengths in the way described in Engmaier & Gerhard (1997). A typical example of results obtained with 2D SPH is shown in figure 6.

### 3.2.2 Two-dimensional Piecewise Parabolic Method

A 2D PPM code called CMHOG2 was provided by P. Teuben. The code uses PPM in the Lagrangian remap formalism, and includes isothermal hydrodynamics in polar coordinates. The code is based on that described in Piner, Stone & Teuben (1995); for a description of the Piecewise Parabolic Method, see Colella & Woodward (1984).

Results from calculations of the standard model and a model with  $m = 4$  are shown in figure 7. Sharp shocks were formed as expected, and the strength of the shocks fades towards the corotation radius. Results from further calculations, with variations of the strength  $F$  and the pattern speed  $\Omega_P$ , were very similar.

Results from the standard model are compared to semi-analytical results in figures 8, 9 and 10, at radii  $R = 10$ , 7 and 13 kpc, respectively. Recall that a period of  $2\pi$  in  $\eta$  always corresponds to the passage from one arm to the next, regardless of the number of arms. The agreement is excellent in all three cases, and the narrow density peaks are reproduced by the grid code. The sharp shock front is spread over several zones, but it is reproduced much more

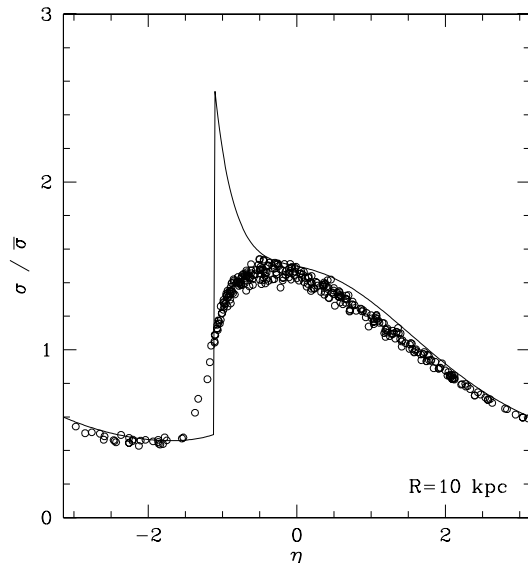


**Figure 6.** Density profile  $\sigma(\eta)$  of the standard model at  $R = 10$  kpc as computed by the semi-analytical method (solid line), compared to results extracted from a 2D SPH calculation (circles).

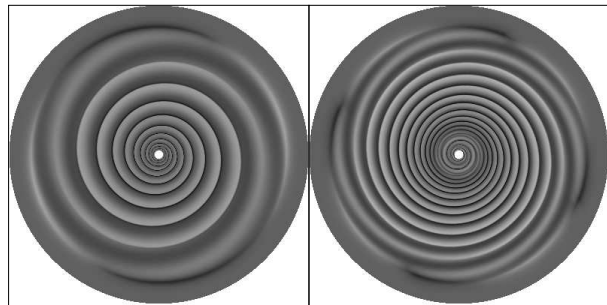


**Figure 7.** Surface density maps from calculations of the standard model (left) and with  $m = 4$  (right) at  $t = 1$  Gyr. The maximum radius is 20 kpc.

accurately than in the SPH code. All the density profiles show some small oscillations in the density downstream of the shock. At  $R = 13$  kpc, there is once again a discrepancy between the semi-analytical prediction and the calculation result, probably due to the proximity of the 6:1 ultraharmonic resonance.

The agreement with the semi-analytical profiles improves as the resolution of the grid-code is increased. Figure 8 shows the result obtained with 150 radial zones, compared to the full 600, for comparison. This trend held up to the limits of available resolution, and presumably, with more computing resources, ever more accurate agreement could be achieved.

Figure 11 shows a comparison at 10 kpc with the calculation using  $m = 4$ . The general shape of the profile is again well-represented, but in this case the position of the shock is slightly further upstream in the grid-code result than the semi-analytical prediction. This is a general result when  $m = 4$ . The reason for the difference is not clear. The number of grid zones covering one arm is half that in the  $m = 2$  calculations, so doubling the resolution might remove

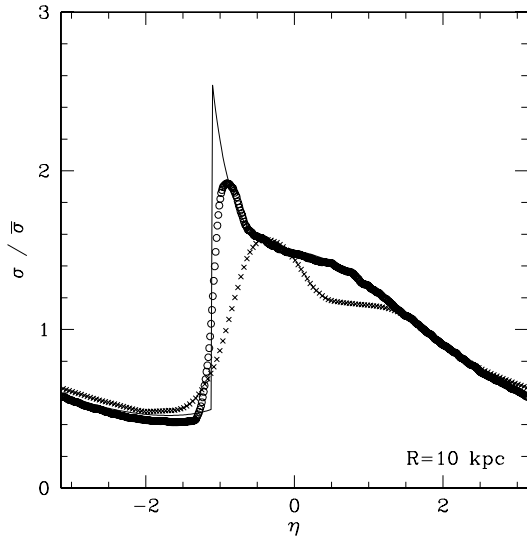


**Figure 8.** Density profile  $\sigma(\eta)$  of the standard model at  $R = 10$  kpc as computed by the semi-analytical method (solid line), compared to results from the grid-code calculation (circles). Also shown are the results from the same calculation with 1/4 the number of radial zones (crosses).

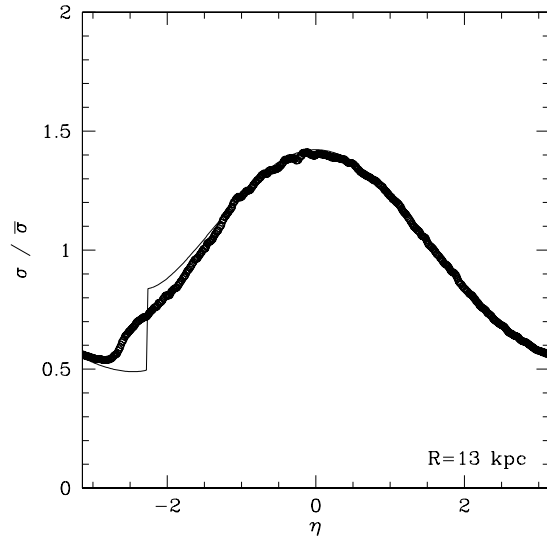


**Figure 10.** Comparison as in figure 8, at  $R = 13$  kpc. This radius is in the base-subsonic region, and is close to the 6:1 resonance.

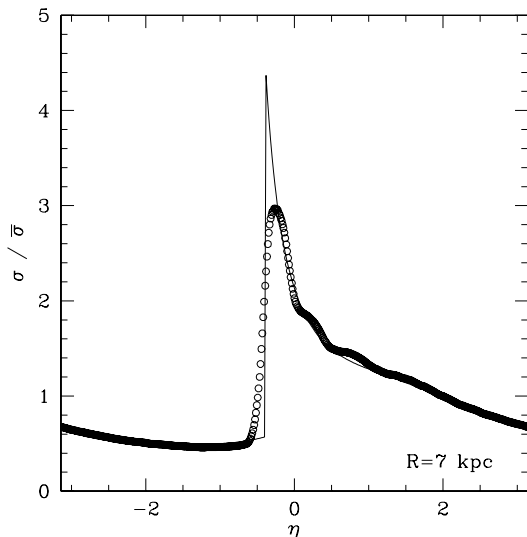


**Figure 9.** Comparison as in figure 8, at  $R = 7$  kpc.

the offset. Such high resolution is impractical at time of writing. However, when the angular resolution is halved instead, the predicted shock location is not obviously changed, which suggests that the effect is not resolution dependent.

The shock location in the results corresponds very closely to the predicted location from the semi-analytical results in all cases where  $m = 2$ , at radii between the inner Lindblad resonance and the start of the base-subsonic region. Figure 12 plots the measured location of the shock as a function of radius, from the calculation of the standard

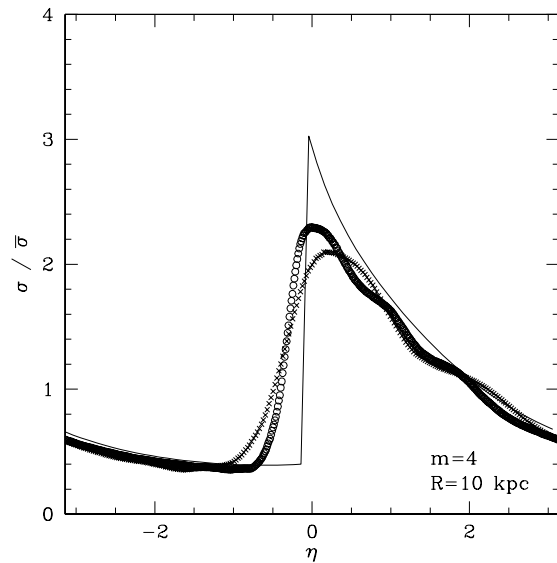


**Figure 11.** Comparison as in figure 8 with  $m = 4$ . The result with half the angular resolution is also shown (crosses).

model. The positions predicted from the semi-analytical theory are also shown, where they can be found. In figure 13, the results for the model with  $m = 4$  are given. When  $m = 2$ , there is excellent agreement between the two. At large radii, in the base-subsonic region, the shocks become so weak that the shock location in the grid-code results cannot be determined accurately. The comparison with  $m = 4$  shows that the grid-code consistently places the shock further upstream than the prediction of the semi-analytical theory, as discussed above.

Similar comparisons were made from calculations using  $F = 0.03$  and  $\Omega_P = 19.5 \text{ km s}^{-1}$ , and in both cases, very

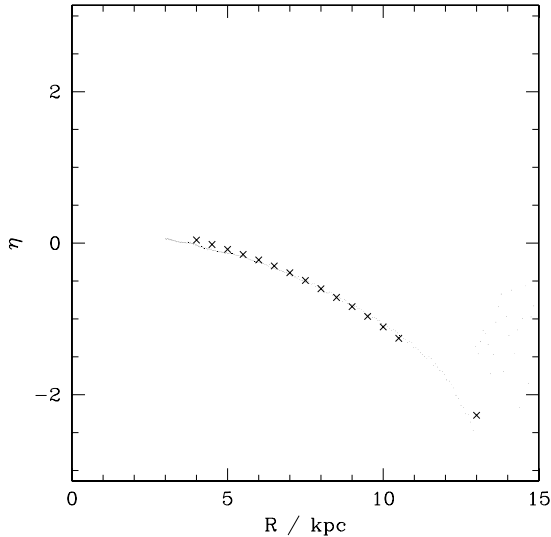


**Figure 12.** Shock location vs. radius in the standard model, as measured from the grid-code calculation (points) and predicted from the semi-analytical results (crosses).

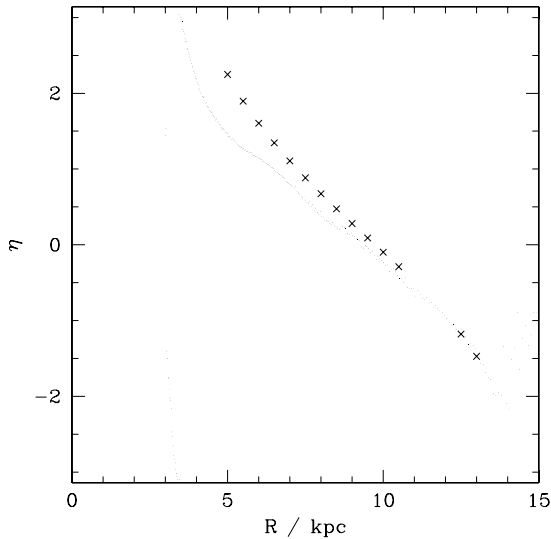


**Figure 13.** Shock location vs. radius in the  $m = 4$  model, as measured from the grid-code calculation (points) and predicted from the semi-analytical results (crosses).

close agreement was seen. Numerical results confirm the predictions of the semi-analytical method in parameter regimes where such results are possible. Grid-code calculations were also carried out for parameters where no semi-analytical solutions exist, such as those with larger inclinations (i.e. more open arms) or lower sound speeds. In general, under these conditions, the gas failed to settle to a steady solution, and a much more complex structure was seen involving multiple shocks and significant secondary peaks in the density. These more complicated cases are left for further investigation.

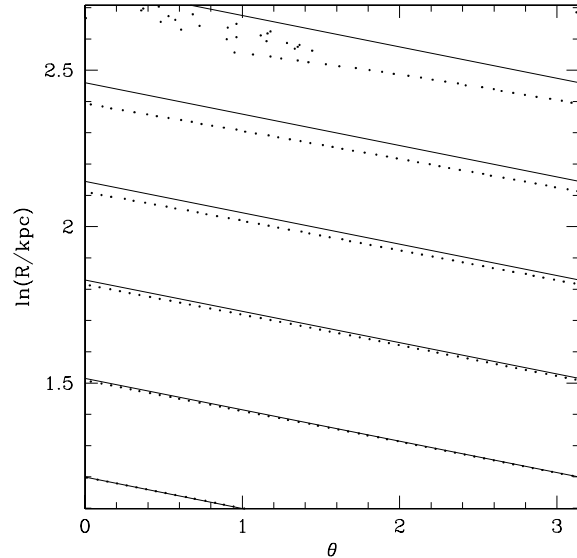


**Figure 14.** Shock location with  $m = 2$  measured from the grid-code calculation (points) over the range 5–15 kpc. Potential minima are marked as lines. Only the range  $0 < \theta < \pi$  is shown since the grid-code only calculates half the plane.

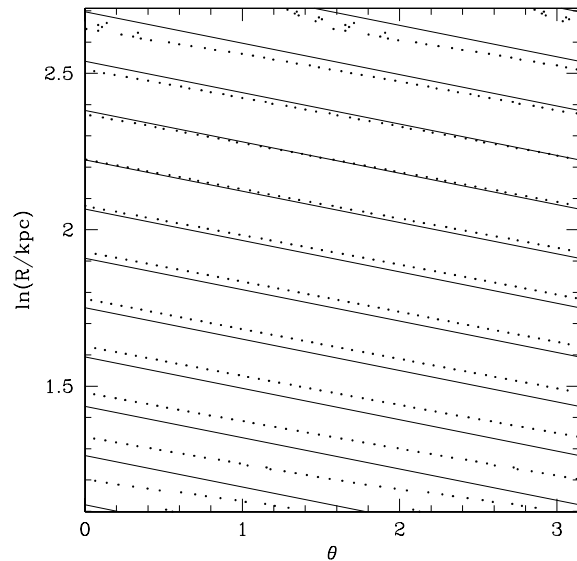


**Figure 15.** Plot as in figure 14, with  $m = 4$ .

In figure 14, the shock location with  $m = 2$  is plotted as  $\ln R$  vs.  $\theta$  and compared to the potential minima, which are of course straight lines on such a plot. The shocks are near the minima at small radii, and move toward the maxima as corotation is approached, until they become too small for the grid-code to locate and the points scatter. The result with  $m = 4$  is shown in figure 15. In this case, the shocks move from the maxima at small radii to cross the minima, and continue to move to the next maxima. The shocks thus complete a transition from one arm to the next.

## 4 SPIRAL ARM COMPONENTS AND THE OFFSET FUNCTION

### 4.1 Shock locations

The ‘offset function’ referred to in this paper,  $\Theta(R)$ , is defined as

$$\Theta = m(\theta_{\text{shock}} - \theta_{\text{min}})$$

where the potential minimum lies at angle  $\theta_{\text{min}}$  and the shock is at angle  $\theta_{\text{shock}}$ . (The offset is defined to lie in the range  $-\pi < \Theta \leq \pi$ ). For tightly wound spirals, in which the streamlines are almost circular, this is almost equivalent to  $\eta_{\text{shock}} - \eta_{\text{min}}$ . Since  $\eta$  is defined in such a way that the minima of the potential correspond to  $\eta = 0$  (equation 1),  $\eta_{\text{min}} \equiv 0$ , and so

$$\Theta = \eta_{\text{shock}}.$$

This very convenient result allows the offset to be read directly from density profiles  $\sigma(\eta)$ , whether generated semi-analytically or in numerical calculations.

The value of  $\Theta(R)$  is difficult to predict without performing a full calculation. It will be expected to vary with the relative velocity of the gas and the potential, as it is the deceleration and acceleration of the gas that causes a shock to form in the first place. The offset should, therefore, vary systematically with radius in a galaxy, since the relative velocity  $R(\Omega - \Omega_{\text{P}})$  decreases with increasing radius towards corotation.

The existence and variation of this offset have been noted before. Roberts (1969) noted, from calculations of semi-analytical solutions, that ‘the shock lies just on the inner side of the background [i.e. potential] spiral arm’, indicating that  $\Theta$  was generally small and negative. Shu et al. (1972) report a value of  $\Theta = -72^\circ$  for their calculations of the flow in the solar neighbourhood. Yuan & Grosbøl (1981) generated synthetic colour profiles across a spiral arm, based on semi-analytical solutions of the flow. They state that ‘the shock ... always occurs on the inner side of the potential minimum’ ( $\Theta < 0$ ), and for their calculations adopt a constant value  $\Theta = -30^\circ$  (in their paper  $\Theta$  is given the symbol  $\Delta_0$ ). This result, that  $\Theta$  should be small and negative, is often tacitly assumed to be correct in discussions of spiral arms. For example, Seigar & James (1998) state that ‘the fact that dust lanes [associated with shocks] appear on the trailing [i.e. upstream, inside corotation] edges of [potential] arms is itself evidence for the large-scale shock scenario’. The systematic variation of  $\Theta$  with radius, however, does not seem to have been discussed in the literature.

Elmegreen & Thomasson (1993) performed particle-based simulations of a galaxy, in which gas clouds and stars were represented by interacting particles. In the somewhat open ( $\sin i \simeq 0.34$ ) spiral arms that formed in the disc, they found that ‘the location of the [gas] shock front changes from the inside of the [stellar] arm inside corotation to the outside of the arm outside corotation’, that is,  $\Theta < 0$  inside corotation and  $\Theta > 0$  outside. This general trend is in agreement with the usual predictions discussed above. However, the shock front is very poorly resolved in their results, and a detailed examination of  $\Theta$  would not be possible.

Kikuchi, Korchagin & Miyama (1997) discuss angular separations between different arm components arising in an unstable galactic disc. Their analysis differs from ours in

that they constrain all components to share a common velocity field, thus negating the possibility of shocks in the gas phase. They nevertheless find that the ordering of the gas and stellar arms reverses at corotation, and suggest the utility of this result in constraining the location of corotation in observed spirals.

### 4.2 Observational characteristics of spiral arms

In discussing the observational characteristics of a model spiral galaxy, it is very important to be precise about what is meant by an ‘arm’. Since a spiral arm will affect different components of the disc in different ways, arms traced by one phenomenon may appear very different to arms traced by another.

In general, one expects to see *three* spiral arm patterns. The first is that traced by the potential minima, or the maximum surface density. In fact, these two definitions will not coincide exactly, since the potential is always more curved in  $R$  than the underlying density. The effect is that the potential minima are slightly more tightly wound than the peaks of the surface density, but we will disregard this difference here. These arms, created by the mass variations in the old stellar population, are expected to have a smoothly varying structure. The second set of arms is traced by the shock front of the gas (where it exists). In strong shocks, this will also represent the maximum gas density. Since dust is generally taken to be a tracer of shocked gas, these arms will also be traced by dust lanes. The third set of arms is the region of enhanced star formation. The existence of this third arm, linked to the other two, relies on the assumption that the shocked gas promotes star formation in the ISM. There will then be some finite ‘onset’ time, during which the early stages of star formation take place. This is followed by an increased density of young stars, H II regions and so on, which will trace the region of star formation. This third set of arms would, therefore, be expected to occur downstream of the second. These three arms are labelled, in this paper, the P-arm (for Potential), the D-arm (for Dust) and the SF-arm (for Star Formation).

With this definition,  $\Theta$  refers to the offset between the P-arm and the D-arm, irrespective of the existence or location of any SF-arm. If  $\Theta(R)$  is a constant, then the D-arms will be identical to the P-arms, but rotated by an angle  $\Theta/m$ , and the two will therefore have identical pitch angles. If, however,  $\Theta$  becomes more negative with increasing radius (e.g. the shock moves further upstream of the potential minimum at larger radii), then the D-arm should be more tightly wound than the P-arm.

The relative pitch angles of the D-arm and SF-arm are also likely to be different. If the assumption of a constant *time* offset from the D-arm to the SF-arm (associated with the onset of star formation) is made, then the angular offset will be proportional to the relative angular velocity of the gas  $\Omega - \Omega_{\text{P}}$ . Since this decreases to zero as radii approach corotation, the offset will also decrease to zero. The SF-arm would therefore be expected to be more tightly wound than the D-arm.

Figure 16 is a diagram of the three arms, in the particular case that  $\Theta$  becomes more negative with radius and the star formation onset time is constant. Under both of these circumstances, the pitch angles of the arms are expected



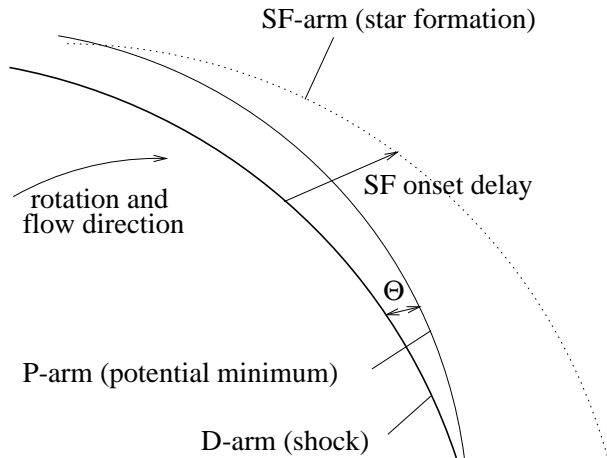


**Figure 16.** Diagram of the three types of spiral arm and their separations. In this diagram  $\Theta$  becomes more negative with radius, so that the D-arm is more tightly wound than the P-arm. The star formation time delay is constant, but since the relative velocity of the gas to the P-arm is smaller at larger radii, the angular delay is smaller. Consequently the SF-arm is more tightly wound than the D-arm.

to follow  $i_P > i_D > i_{SF}$ . Visser (1980a) makes the point that a constant  $\Theta$  is required for the P-arms and D-arms to have the same pitch angle, and comments that in M81 the tendency is for both the ‘gas and dust’ (D-arms) and ‘H II regions and young stars’ (SF-arms) to be tighter than the potential arms.

The three types of spiral arm are observed in different ways. Observing the P-arm requires observations at longer wavelengths, that isolate the older stellar population in the disc. These arms would probably, therefore, be observed as peaks in the K or I bands. The D-arms, defined by the locations of shocks, should be traced by dust lanes or radio emission ridges. If these arms correspond to the peaks of the gas density, then they should also be traced by peaks of CO emission (and other tracers of dense molecular gas). Finally, the SF-arms can be traced by bluer light, such as the B band, or by H $\alpha$  emission from H II regions. Determining the location and extent of the SF-arms is hampered by the effects of dust reddening.

Generally, the strongest CO emission is seen to coincide with the dust lanes and nonthermal ridges, in M51 for example (Lo et al. 1987), and all of these are displaced from the peak of H $\alpha$  emission (Tilanus et al. 1988; Nakai et al. 1994). The offset from CO peaks to H II regions is seen in most grand design spirals, such as M31 (Ichikawa et al. 1985). More recent observations have detected a sequence of  $^{12}\text{CO}$  to  $^{13}\text{CO}$  to H $\alpha$  across an arm in M51 (Tosaki et al. 2002), supporting the idea of a gradual collapse of molecular clouds to higher densities in the onset of star formation. One exception is the observation of Lord & Kenney (1991) that peaks of CO emission are offset from the dust lanes in an arm of M83, which they attribute to dense clouds penetrating through the shock layer while a more diffuse component is compressed to a shock.

In principle, therefore, the positions of the D-arm and P-arm can be observed. This would then allow a direct measurement of  $\Theta(R)$ . The resulting data will enable constraints

to be placed on the parameters of the galaxy’s spiral structure, as discussed in the next section.

## 5 LOCATING THE COROTATION RADIUS IN GALAXIES

The determination of the corotation radius (or, equivalently, the pattern speed) in spiral galaxies has been attempted by various methods for various galaxies. The assumption that a pattern speed exists at all implies that a rigidly rotating spiral potential is present.

The simplest way to estimate the corotation radius is to associate it with the maximum extent of observed spiral arms. The idea that star formation is promoted by the shock compression means that at corotation (where there can be no shock compression), star formation should be absent. The radius of the outermost H II region has therefore been used as an estimate of the corotation radius (e.g. Rots 1975, in M81). This method is not reliable, since longer exposures tend to reveal further features at larger radii in galaxies, and H II regions may exist outside corotation. An alternative, but similar, approach is to associate the inner edge of observed spiral features with the inner Lindblad resonance, on the basis that spiral waves are not expected to extend beyond the Lindblad resonances. However, several investigations have discussed the possibility of spiral patterns extending within the inner Lindblad resonance (Elmegreen et al. 1998; Englmaier & Shlosman 2000; Martini et al. 2003), so this method is unlikely to be accurate without detailed modelling. More sophisticated analyses associate various observational features with a range of resonances in a galaxy to constrain the corotation radius (Elmegreen & Elmegreen 1990; Elmegreen, Elmegreen & Montenegro 1992).

Alternatively, if the velocity curve (and preferably other parameters such as velocity dispersions and mass models) of a galaxy are known, then a corresponding spiral structure can be simulated, based on a specified pattern speed and the spiral density wave theory. The pattern speed can then be adjusted until the best fit is achieved. This approach was taken by Visser (1980b) in an analysis of M81, and more recently for several galaxies (Kranz, Slyz & Rix 2003).

Another approach makes use of the predicted radial variations in the arm amplitude. These are associated with interference between outward and inward travelling spiral waves, and fitting the oscillations can locate corotation (Elmegreen, Seiden & Elmegreen 1989). The ‘modal’ approach (Bertin et al. 1989) involves examining the full range of normal modes of the galactic disc and their relative amplitudes. The technique has been applied to M81 (Lowe et al. 1994). Other methods include: matching radial oscillations in the velocity curve to predicted velocity fields (Yuan 1969); the ‘geometric phase’ method (Canzian & Allen 1997), which associates corotation with a shift from singly to triply symmetric structure in the velocity field; and the integrated continuity equation method (Westpfahl 1998), in which asymmetries in the observed disc are exploited to constrain  $\Omega_P$ .

Of course, values determined by different methods rarely agree exactly; table 2 lists pattern speeds derived for the spiral pattern in M81 from a variety of sources in the

**Table 2.** Some pattern speeds of M81 reported in the literature.

$\Omega_P / \text{km s}^{-1} \text{kpc}^{-1}$	Source
17.4	Shu, Stachnik & Yost (1971)
26.4	Roberts, Roberts & Shu (1975)
20	Rots (1975)
18.3	Gottesman & Weliachew (1975)
18	Visser (1980a)
20	Berman & Mishurov (1982)
17 $\pm$ 2	Sakhibov & Smirnov (1987)
26	Elmegreen et al. (1989)
24	Lowe et al. (1994)
23.4 $\pm$ 2.3	Westpfahl (1998)

literature. This indicates a spread of some 25% in one of the most studied spiral galaxies.

A commonly suggested method of locating corotation arises from examination of the separate arm components. If star formation occurs at some time offset after the passage of a spiral shock, then the relative location of the D-arm and the SF-arm should be reversed inside and outside corotation. The radius at which these arms cross should, therefore, correspond to corotation. This point is mentioned by Grosbøl & Patsis (1998), but they failed to observe such a crossing.

Dixon (1971) proposed that observations in the B and V bands could allow the variation of stellar age across an arm to be determined, and that corotation should correspond to the radius at which this trend reverses angular direction. Puerari & Dottori (1997) attempted to locate corotation in two galaxies by this method, performing a Fourier analysis on observations in B and I bands. Observational studies of the separations of arm components usually focus on the SF-arm and the P-arm, observing in (for example) B and K bands. Beckman & Cepa (1990) observed in the B and I bands, finding an offset in one galaxy, but too flocculent a structure in another. Grosbøl & Patsis (1998) measured radial variations in the location of SF-arms and P-arms, but conclude that uncertainties in the absolute phase offset between them prevent corotation from being located. Seigar & James (1998) also examined arms in the K and B bands, observing that the SF-arms appear on the convex side of the P-arms as expected, but that the P-arms are more tightly wound than the SF-arms, which is the opposite of the expected result.

All of these investigations are based on observations of the SF-arms. This will always be inherently difficult, since the existence, location and shape of the SF-arm are neither expected, nor observed, to be very regular. As discussed in the introduction, galaxies with regular structure in P-arms will often be classified as flocculent in optical observations, meaning that they do not possess regular SF-arms. As pointed out by Elmegreen (1979), one would expect the stimulation of star formation in shock fronts to be followed by a ‘shuffling’ of material, including feedback from star formation, random structure from the condensation of dense clouds and so forth. The appearance of any SF-arm would therefore be much more irregular, and in the right circumstances will appear entirely flocculent. The observation of these arms is further hampered by the effects of dust obscuration, which can make it difficult to locate their full extent.

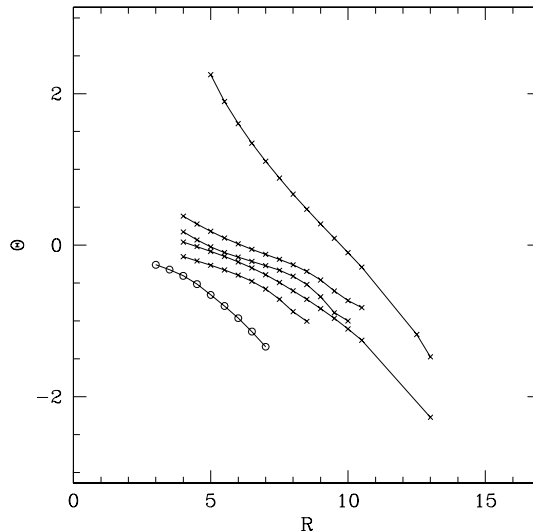


**Figure 17.** Plots of  $\Theta(R)$  with various parameters. Lines marked with crosses correspond to (bottom to top)  $F = 0.03$ , standard model,  $i = 0.15$ ,  $a = 5 \text{ km s}^{-1}$ ,  $m = 4$ . Line with circles corresponds to  $\Omega_P = 19.5 \text{ km s}^{-1} \text{kpc}^{-1}$ .

Furthermore, the unknown quantity of the ‘onset time’ for star formation may in reality be a range of times, leading to star formation occurring at a range of offsets from the shock. The prediction of the large scale shock-induced star formation scenario would be, therefore, that regular P-arms should produce regular D-arms, and any subsequent SF-arms will be irregular and poorly localised.

Observations of the P-arms and D-arms, and the offset  $\Theta$  between them, avoid all such issues and would be expected, in galaxies with a regular spiral potential, to result in a much clearer result. In the next section, the way in which corotation might be constrained from such measurements is described.

### 5.1 Constraining corotation from the shock-potential offset

As has already been seen in figure 12, there is a general trend for  $\Theta$  to vary in two-armed spirals in a specific way. At small radii,  $\Theta$  approaches zero, but as the radius approaches corotation,  $\Theta$  moves toward  $-\pi$ . Even with  $m = 4$ , although  $\Theta$  does not go to zero at small radii, it still moves toward  $-\pi$  with increasing  $R$ . The extrapolation of the curve of  $\Theta$ , in all these cases, roughly indicates the location of corotation.

The form of  $\Theta(R)$  does, of course, depend on the parameters of the spiral potential. However, the extrapolation of  $\Theta$  to find corotation stays approximately unchanged under all such variations. Figure 17 shows the curve for the standard model compared to the alterations  $i = 0.15$ ,  $F = 0.03$ ,  $a = 5 \text{ km s}^{-1}$ ,  $m = 4$  and  $\Omega_P = 19.5 \text{ km s}^{-1} \text{kpc}^{-1}$ . Corotation is located at 17 kpc in all of these models except the last, in which it is at 11.3 kpc. The shapes of all the curves indicate corotation to be in the range 15–20 kpc, except the curve at higher  $\Omega_P$  which correctly indicates a smaller radius of corotation.

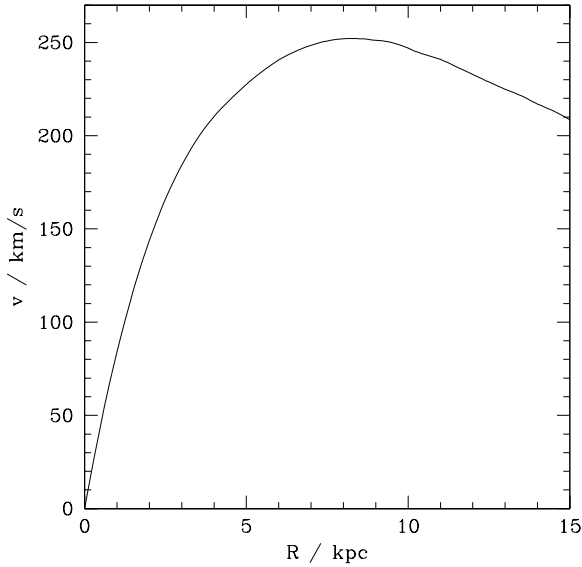


**Figure 18.** Velocity curve used in Shu et al. (1973).

Variations in the velocity curve will also affect the shape of  $\Theta(R)$ . In figure 19, the resulting plots are compared using a flat velocity curve, a rising velocity curve in which  $\epsilon_d^{-1} = 10$  kpc (rather than 1.5 kpc), and the velocity curve used in Shu et al. (1973), which is peaked at around 8 kpc, and shown in figure 18. The values corresponding to  $\Omega_P = 19.5$  km s<sup>-1</sup> kpc<sup>-1</sup> are also shown. Since each of these velocity curves places corotation at a different radius, the values are plotted against  $R/R_{\text{corotation}}$  in this figure. Again, in all cases the approximate position of corotation is indicated by the extrapolation of the curve.

Probably the most difficult parameter to constrain in a spiral galaxy is the relative strength  $F$  of the spiral perturbations. In the standard model, this takes the value 5% at  $R = 8.5$  kpc, and varies as  $R \exp(-\epsilon_s R)$ . In figure 20, the shock locations obtained using a constant strength  $F(R)$ , at values 3%, 5% and 10%, are shown. This figure indicates that the spiral strength introduces the greatest uncertainty into the location of corotation. Generally, weaker spirals will form shocks further upstream at smaller radii than stronger spirals. If the strength of the spiral perturbation varied systematically across a galactic disc, for example increasing from 3% to 10% (or vice versa), the extrapolation of  $\Theta$  could indicate an inaccurate value for corotation.

## 5.2 Example results and accuracy

To assess the approximate accuracy of the method, we consider in this section how the semi-analytical results in figures 17, 19 and 20 may be used, in conjunction with observational data, to constrain the location of corotation in spiral galaxies. We therefore begin with 10 sets of data  $\Theta(R)$  for  $m = 2$ . The general idea is to extrapolate the downward-curving trend to the point  $\Theta = -\pi$ , which forms the estimate for corotation.

The radial range over which we have managed to obtain semi-analytic solutions depends on the model parameters (e.g. arm strength, rotation curve), so that these parameters

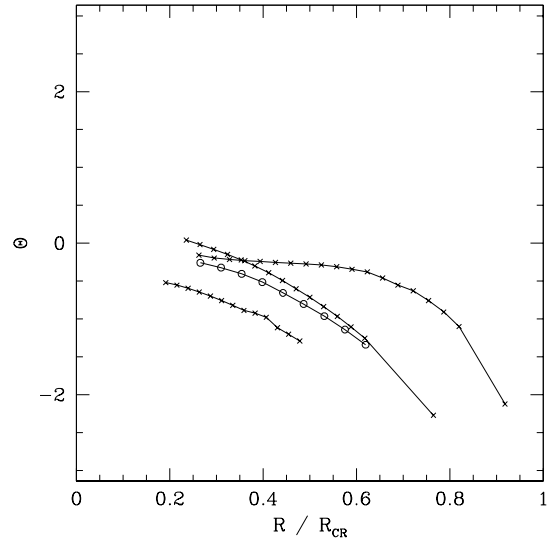


**Figure 19.** Plots of  $\Theta(R)$ , plotted against radius relative to corotation, for various parameters. Lines marked with crosses correspond to (left to right)  $\epsilon_d^{-1} = 10$  kpc, standard model, velocity curve from figure 18. Line marked with circles corresponds to  $\Omega_P = 19.5$  km s<sup>-1</sup> kpc<sup>-1</sup>.

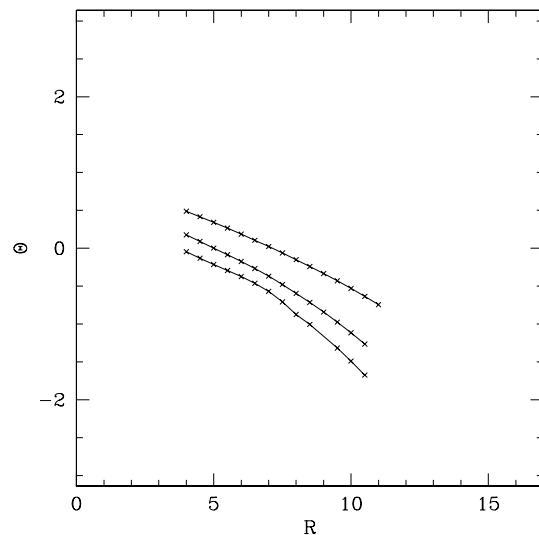


**Figure 20.** Plots of  $\Theta(R)$  for models using a constant  $F$  of (bottom to top) 0.03, 0.05 and 0.1.

affect the range in  $\Theta(R)$  for which we have solutions in each case. Estimates will be more accurate where a larger  $\Delta\Theta$  is available. We wish to assess the approximate accuracy of this method as a function of  $\Delta\Theta$ .

To this end, we analysed the results at values of  $\Delta\Theta$  in steps of  $\pi/8$  up to the largest value covered by the data. For each value of  $\Delta\Theta$ , only those curves were included whose results cover at least that range, and only the points (at small radii) within that range were used. Thus, at small

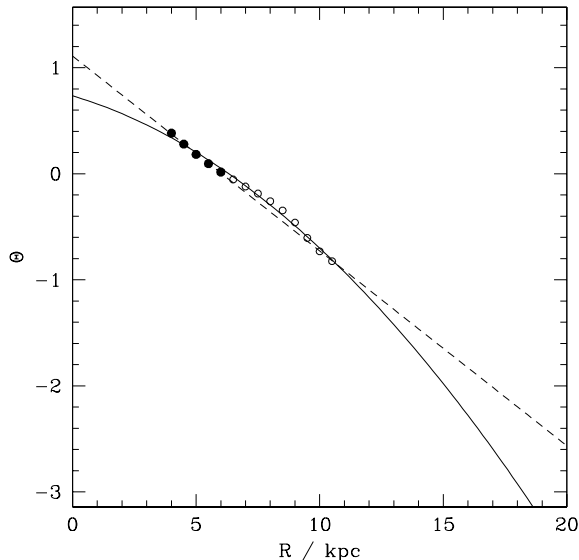


**Figure 21.** The extrapolation of the results with  $a = 5 \text{ km s}^{-1}$  at two values of  $\Delta\Theta$ . At  $\Delta\Theta = \pi/8$ , only the first five points constitute the data (solid circles). The resulting quadratic fit has the wrong curvature, so a linear fit is used (dashed line). At  $\Delta\Theta = \pi/2$ , all the data are included, and the quadratic fit estimates the corotation radius at 18.6 kpc.

$\Delta\Theta$ , all the curves can be extrapolated, but only the first part of each will be used. At large  $\Delta\Theta$ , only a few of the curves have sufficient data to produce a result, but they will be more accurate.

Any set of data clearly needs to show a decrease in  $\Theta$  with  $R$  as a minimum requirement for this method to be applied. The simplest extrapolation is to apply a least-squares quadratic fit to the points. In some cases, the data curve toward positive  $\Theta$  over some sections, in which case a quadratic fit does not extrapolate to  $\Theta = -\pi$ . To avoid this problem, if the coefficient of  $R^2$  in the quadratic fit is positive, we use a linear fit instead. Once a fit has been chosen, the corotation radius is estimated as the intersection of the fit with  $\Theta = -\pi$ . Figure 21 illustrates some fits for the data with  $a = 5 \text{ km s}^{-1}$ .

The scatter in the resulting predicted values for corotation over the 10 sets of data gives an indication of the accuracy of this method. The results are plotted in figure 22 for all values of  $\Delta\Theta$ . At an optimal value of  $\Delta\Theta \simeq 3\pi/8$  to  $4\pi/8$ , most of the data sets cover a sufficient range to be included, and the spread is some 25%. We estimate, therefore, that this method should be accurate to around 25% if a sufficiently large  $\Delta\Theta$  is available in the observed data, and that  $\Delta\Theta \gtrsim \pi/4$  is a reasonable guide to this requirement.

## 6 CONCLUSIONS

In this paper, we re-examine the response of an isothermal gas disc to a model spiral potential, leading to a large-scale flow containing a single shock. The established semi-analytical method was compared to results from numerical techniques, with good agreement within the limitations of each method. We found that:

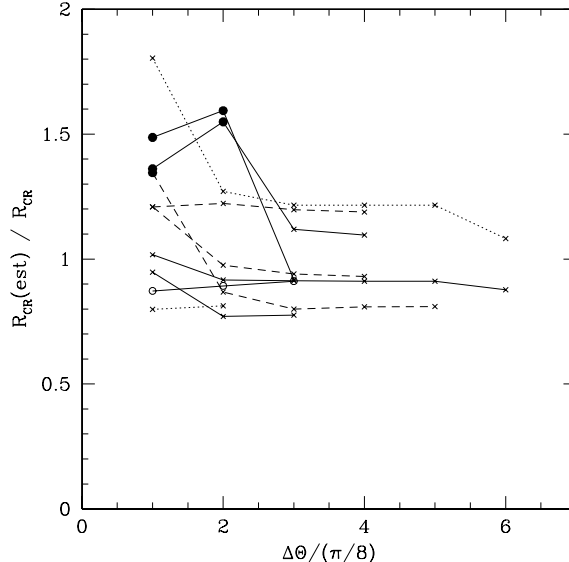


**Figure 22.** The ratio of predicted to actual corotation radius for all the data sets, as a function of  $\Delta\Theta$ . Solid lines with crosses correspond to (bottom to top at left end)  $F = 0.03$ , standard model,  $a = 5 \text{ km s}^{-1}$ ,  $i = 0.15$ . The solid line with circles corresponds to  $\Omega_P = 19.5 \text{ km s}^{-1} \text{ kpc}^{-1}$ . Dashed lines are models with constant  $F$  with values (bottom to top at right end) 3%, 5%, 10%. Dotted lines are alternative velocity curves (lower:  $\epsilon_d^{-1} = 10 \text{ kpc}$ , upper: figure 18). Solid circles indicate results where a linear (rather than quadratic) extrapolation was used.

(i) Results from two-dimensional SPH fail to resolve the shock sufficiently sharply to determine its location. More work on the details of the SPH implementation may improve results.

(ii) Much better results were obtained with the PPMLR code CMHOG2.

(iii) In parameter regimes where a semi-analytical solution cannot be found, in general the numerical results failed to show a simple single-shock solution.

We discuss the appearance of spiral arms in galaxies, and the existence of three separate arms, the P-arm (in the stellar disc, approximately tracing the gravitational Potential), the D-arm (the shock as traced by Dust) and the SF-arm (an arm traced by enhanced Star Formation). Even in galaxies classified as optically flocculent, a regular structure in the P-arms and D-arms should be common. The angular offset  $\Theta(R)$  between the D-arm and P-arm is proposed as an observable function, avoiding all the difficulties inherent in tracing the shape and location of the SF-arm.

Finally, we show how this function could be extrapolated to provide an estimate of the corotation radius, and assess the accuracy of the method as a function of the range  $\Delta\Theta$  available in the observations. We estimate that given  $\Delta\Theta \gtrsim \pi/4$ , the method is accurate to around 25%.

## ACKNOWLEDGEMENTS

Thanks are due to Peter Teuben for providing the CMHOG2 code. Advice and comments are acknowledged from Jim

Pringle, Ron Allen, Steve Lubow, Jerry Sellwood, Eve Ostriker and Jim Stone. Thanks are also due to Jonathan Gair for suggesting the change of variables to avoid the singularity in the semi-analytical equations. Finally, we thank the referee for useful comments, and for suggesting the addition of a quantitative assessment of the accuracy of the method.

## REFERENCES

- Beckman J. E., Cepa J., 1990, *A&A*, 229, 37  
 Berman S. L., 2002, in *ASP Conf. Ser. 275: Disks of Galaxies: Kinematics, Dynamics and Perturbations Simulations of Dual Morphology in Spiral Galaxies*. pp 301–304  
 Berman V. G., Mishurov Y. N., 1982, *AZh*, 59, 1055  
 Bertin G., Lin C. C., Lowe S. A., Thurstans R. P., 1989, *ApJ*, 338, 78  
 Block D. L., Bertin G., Stockton A., Grosbøl P., Moorwood A. F. M., Peletier R. F., 1994, *A&A*, 288, 365  
 Canzian B., Allen R. J., 1997, *ApJ*, 479, 723  
 Colella P., Woodward P. R., 1984, *J. Comp. Phys.*, 54, 174  
 Contopoulos G., Grosbøl P., 1986, *A&A*, 155, 11  
 Cowie L. L., 1980, *ApJ*, 236, 868  
 Dixon M. E., 1971, *ApJ*, 164, 411  
 Elmegreen B. G., 1979, *ApJ*, 231, 372  
 Elmegreen B. G., Elmegreen D. M., 1990, *ApJ*, 355, 52  
 Elmegreen B. G., Thomasson M., 1993, *A&A*, 272, 37  
 Elmegreen B. G., Seiden P. E., Elmegreen D. M., 1989, *ApJ*, 343, 602  
 Elmegreen B. G., Elmegreen D. M., Montenegro L., 1992, *ApJS*, 79, 37  
 Elmegreen B. G., Elmegreen D. M., Brinks E., Yuan C., Kaufman M., Klaric M., Montenegro L., Struck C., Thomasson M., 1998, *ApJ*, 503, L119  
 Elmegreen D. M., Elmegreen B. G., 1984, *ApJS*, 54, 127  
 Englmaier P., Gerhard O., 1997, *MNRAS*, 287, 57  
 Englmaier P., Shlosman I., 2000, *ApJ*, 528, 677  
 García Gómez C., Athanassoula E., 1993, *A&AS*, 100, 431  
 Gittins D., 2003, Ph.D. Thesis  
 Gottesman S. T., Weliachew L., 1975, *ApJ*, 195, 23  
 Grosbøl P. J., Patsis P. A., 1998, *A&A*, 336, 840  
 Ichikawa T., Nakano M., Tanaka Y. D., Saito M., Nakai N., Sofue Y., Kaifu N., 1985, *PASJ*, 37, 439  
 Kaplan S. A., Pikelner S. B., 1974, *ARA&A*, 12, 113  
 Kennicutt R. C., 1981, *AJ*, 86, 1847  
 Kennicutt R. C., Hodge P., 1982, *ApJ*, 253, 101  
 Kikuchi N., Korchagin V., Miyama S. M., 1997, *ApJ*, 478, 446  
 Kranz T., Slyz A., Rix H., 2003, *ApJ*, 586, 143  
 Lin C. C., Yuan C., Shu F. H., 1969, *ApJ*, 155, 721  
 Lo K. Y., Ball R., Masson C. R., Phillips T. G., Scott S., Woody D. P., 1987, *ApJ*, 317, L63  
 Lord S. D., Kenney J. D. P., 1991, *ApJ*, 381, 130  
 Lowe S. A., Roberts W. W., Yang J., Bertin G., Lin C. C., 1994, *ApJ*, 427, 184  
 Ma J., 2002, *A&A*, 388, 389  
 Martini P., Regan M. W., Mulchaey J. S., Pogge R. W., 2003, *ApJS*, 146, 353  
 Nakai N., Kuno N., Handa T., Sofue Y., 1994, *PASJ*, 46, 527  
 Piner B. G., Stone J. M., Teuben P. J., 1995, *ApJ*, 449, 508  
 Puerari I., Dottori H., 1997, *ApJ*, 476, L73  
 Roberts W. W., 1969, *ApJ*, 158, 123  
 Roberts W. W., Roberts M. S., Shu F. H., 1975, *ApJ*, 196, 381  
 Rots A. H., 1975, *A&A*, 45, 43  
 Sakhibov F. K., Smirnov M. A., 1987, *Soviet Ast.*, 31, 132  
 Schweizer F., 1976, *ApJS*, 31, 313  
 Seigar M. S., James P. A., 1998, *MNRAS*, 299, 685  
 Seigar M. S., Chorney N. E., James P. A., 2003, *MNRAS*, 342, 1  
 Shu F. H., Milione V., Gebel W., Yuan C., Goldsmith D. W., Roberts W. W., 1972, *ApJ*, 173, 557  
 Shu F. H., Milione V., Roberts W. W., 1973, *ApJ*, 183, 819  
 Shu F. H., Stachnik R. V., Yost J. C., 1971, *ApJ*, 166, 465  
 Thornley M. D., 1996, *ApJ*, 469, L45  
 Tilanus R. P. J., Allen R. J., van der Hulst J. M., Crane P. C., Kennicutt R. C., 1988, *ApJ*, 330, 667  
 Toomre A., 1977, *ARA&A*, 15, 437  
 Tosaki T., Hasegawa T., Shioya Y., Kuno N., Matsushita S., 2002, *PASJ*, 54, 209  
 Visser H. C. D., 1980a, *A&A*, 88, 149  
 Visser H. C. D., 1980b, *A&A*, 88, 159  
 Westpfahl D. J., 1998, *ApJS*, 115, 203  
 Yuan C., 1969, *ApJ*, 158, 871  
 Yuan C., Grosbøl P., 1981, *ApJ*, 243, 432

## APPENDIX A: METHOD FOR LOCATING SEMI-ANALYTICAL SOLUTIONS

In this appendix, the method for locating solutions in the semi-analytical approach is described for convenience. The method is almost the same as that described in Shu et al. (1972) and Roberts (1969).

The differential equations describing the response of the gas, along a streamline with average radius  $R_0$ , are as follows:

$$\frac{\partial u_{\eta 1}}{\partial \eta} = U(u_{\eta 0} + u_{\eta 1}) \frac{2u_{\xi 1} - FR_0\Omega \sin i}{(u_{\eta 0} + u_{\eta 1})^2 - a^2}$$

$$\frac{\partial u_{\xi 1}}{\partial \eta} = -V \frac{u_{\eta 1}}{u_{\eta 0} + u_{\eta 1}}$$

where

$$u_{\eta 0} = R_0(\Omega - \Omega_P) \sin i$$

$$u_{\xi 0} = R_0(\Omega - \Omega_P) \cos i$$

$$U = \frac{\sin i}{m} R_0 \Omega$$

$$V = \frac{\sin i}{m} \frac{d}{dR} (R^2 \Omega) = \frac{\sin i}{m} \frac{R_0 \kappa^2}{2\Omega}.$$

The resulting gas density  $\sigma = \sigma_0 + \sigma_1$  relative to the unperturbed density  $\sigma_0(R)$  is given by

$$(\sigma_0 + \sigma_1)(u_{\eta 0} + u_{\eta 1}) = \sigma_0 u_{\eta 0}.$$

It is convenient to transform these equations into dimensionless form with  $(u_{\eta 1}, u_{\xi 1})$  replaced by the dimensionless  $(u, v)$  defined by

$$u = \frac{u_{\eta 1}}{\sqrt{2UV}}$$

$$v = \frac{u_{\xi 1}}{V}$$

by first defining the dimensionless parameters

$$f = \frac{FR_0\Omega}{2V}$$

$$\nu = \frac{-u_{\eta 0}}{\sqrt{2UV}}$$

$$x = \frac{a^2}{2UV}$$

so that the final dimensionless equations to be solved are as follows:

$$\frac{\partial u}{\partial \eta} = (u - \nu) \frac{v - f \sin \eta}{(u - \nu)^2 - x} \quad (\text{A1})$$

$$\frac{\partial v}{\partial \eta} = \frac{u}{\nu - u} \quad (\text{A2})$$

For low spiral strength  $F$  or sufficiently high or low sound speed  $a$ , solutions will be entirely supersonic or entirely subsonic, and will not contain a shock. For parameters where  $u_\eta$  crosses the value  $a$ , a shock must exist. The method for locating such a solution containing a single shock (if it exists) is as follows.

As can be immediately seen from equations A1 and A2, singularities occur at three points:  $u = \nu$ ,  $u = \nu - \sqrt{x}$  and  $u = \nu + \sqrt{x}$ . These correspond, respectively, to  $u_\eta = 0$ ,  $u_\eta = -a$  and  $u_\eta = a$ . For a solution flowing through the shock, the first two conditions should never occur, since gas flow through a trailing spiral (inside corotation) should always be moving outward in  $\eta$ . The third singularity corresponds to the sonic point, at which the gas undergoes the transition to supersonic flow after the shock (the gas returns to subsonic flow in the shock itself). The value of  $\eta$  at which this sonic point occurs is denoted  $\eta_{\text{SP}}$ . The singularity at this point is removed as long as  $v(\eta_{\text{SP}}) = f \sin \eta_{\text{SP}}$ . This requirement fixes the boundary conditions; given any guessed value for  $\eta_{\text{SP}}$ , the starting values of  $u$  and  $v$  at this point must be  $u = \nu + \sqrt{x}$  and  $v = f \sin \eta_{\text{SP}}$ .

Solutions are therefore calculated starting at  $\eta_{\text{SP}}$ , and proceeding forward in  $\eta$  (the subsonic branch) and backward in  $\eta$  (the supersonic branch). The determination of the shock location and the procedure for adjusting  $\eta_{\text{SP}}$  to find a solution are described below.

The presence of the singularity at  $\eta_{\text{SP}}$  can create difficulties for numerical integration. Shu et al. (1973) used a series expansion in  $\eta$  around  $\eta_{\text{SP}}$  to overcome this problem. An alternative is to rewrite the equations in new variables, which hide the singularity, as follows (J. Gair, private communication). Start by defining

$$u = \nu + \sqrt{x} + \tilde{u}$$

$$v = f \sin \eta + \tilde{v}$$

and then define

$$\tilde{w} = \tilde{u}^2.$$

The differential equations now become

$$\frac{\partial \tilde{w}}{\partial \eta} = \frac{2(\sqrt{x} \pm \sqrt{\tilde{w}})\tilde{v}}{2\sqrt{x} \pm \sqrt{\tilde{w}}}$$

$$\frac{\partial \tilde{v}}{\partial \eta} = -1 - f \cos \eta - \frac{\nu}{\sqrt{x} \pm \sqrt{\tilde{w}}}$$

where the positive root of  $\tilde{w}$  is taken where  $\tilde{u} > 0$  (i.e. along

the supersonic branch) and the negative root is taken where  $\tilde{u} < 0$  (the subsonic branch). In this form, the equations can be integrated along each branch separately, starting at  $\eta_{\text{SP}}$ , and  $\tilde{w}$  and  $\tilde{v}$  transformed back to find  $u$  and  $v$ . The singularity is hidden and replaced by a forbidden region of phase space, namely the requirement that  $\tilde{w} > 0$ . This will be satisfied so long as the correct boundary condition is used ( $\tilde{v}(\eta_{\text{SP}}) = \tilde{w}(\eta_{\text{SP}}) = 0$ ).

The procedure for locating the shock is as follows. The flow is integrated from  $\eta_{\text{SP}}$  along the supersonic and subsonic branches, to give  $u_{\text{sup}}(\eta)$  and  $u_{\text{sub}}(\eta)$ . Generally, the supersonic branch will eventually return to the singularity at  $u = a$  and cannot be further integrated, while the subsonic branch either tends asymptotically to  $u = 0$ , or also reaches  $u = a$ . If a consistent solution exists, then the shock will terminate both branches before they reach singularities.

For every point along the supersonic branch  $u_{\text{sup}}$ , the isothermal jump conditions can be used to calculate the post-shock velocity  $u_{\text{shock}}$  that the flow would have if the shock were to occur at that particular value of  $\eta$ . Since the shock is perpendicular to the  $\eta$  direction and the gas is isothermal, the jump condition is simply

$$u_{\text{sup}} u_{\text{shock}} = a^2$$

and so the post-shock branch is defined (in terms of the dimensionless parameters) by

$$u_{\text{shock}}(\eta) = \nu + \frac{x}{u_{\text{sup}}(\eta) - \nu}.$$

Through the shock,  $v$  should be continuous, but  $u$  should drop from  $u_{\text{sup}}$  to  $u_{\text{shock}}$ . In a consistent solution, the shock joins the supersonic branch to the subsonic branch at the same value of  $v$ . Therefore, the only consistent location for the shock exists where the post-shock branch crosses the subsonic branch in the  $(v, u)$  plane. This process is shown visually in figure A1. The starting value of  $\eta_{\text{SP}}$  must be adjusted until a shock location appears, at a point on each branch before they reach a singularity. For some parameters, no value of  $\eta_{\text{SP}}$  will produce a shock.

The location of the crossing point is found numerically by minimising  $u_{\text{sub}}(\eta_{\text{sub}}) - u_{\text{shock}}(\eta_{\text{sup}})$  with respect to  $\eta_{\text{sub}}$  and  $\eta_{\text{sup}}$ , which are the values of  $\eta$  on the subsonic and supersonic branch (respectively) at which the shock occurs. The period in  $\eta$  of the solution will therefore be  $\eta_{\text{sup}} - \eta_{\text{sub}}$ . In general, for a given value of the sonic point  $\eta_{\text{SP}}$ , this period will not be  $2\pi$ . The starting value of  $\eta_{\text{SP}}$  must therefore be adjusted, repeating the shock location procedure at each value, until a solution is found with a period of  $2\pi$ . If such a value can be found, it represents the only physical solution to the flow equations, containing one isothermal shock. The density  $\sigma(\eta)$  can be calculated from the values of  $u$ .

Solutions in the base-subsonic region are particularly hard to find. This is because the integrated branches depend very sensitively on the value of  $\eta_{\text{SP}}$ . In some cases, the range of values for which a solution containing a shock exists can have a width of less than  $\pi/1000$ , and so can be difficult to locate. Outside this range, the calculated branches run into singularities too rapidly.

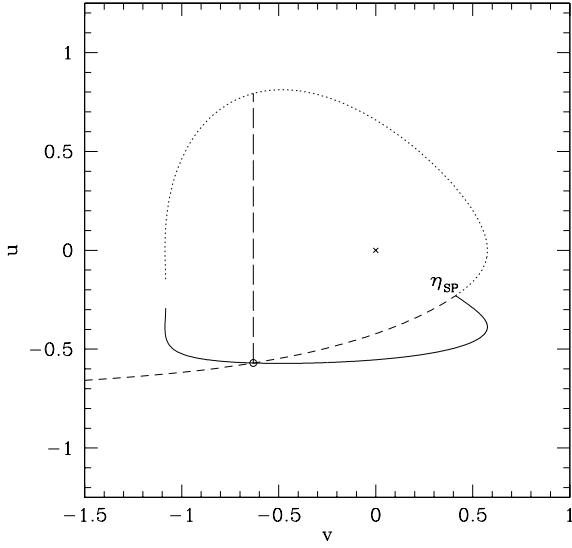


**Figure A1.** The process of locating the shock. Integration starts at the sonic point (labelled  $\eta_{SP}$ ) along the supersonic (dotted) and subsonic (short dashed) branches. The post-shock branch (solid) is calculated for each point along the supersonic branch using the jump conditions. It crosses the subsonic branch at the appropriate location for the shock (circle). The shock, indicated by the long dashed line, closes the velocity curve. Flow proceeds in an anticlockwise direction. The value of  $\eta_{SP}$  should now be adjusted until the period in  $\eta$  of the solution reaches  $2\pi$ . The unperturbed flow corresponds to  $u = v = 0$  (cross).